

Optical properties and local bonding configurations of hydrogenated amorphous silicon nitride thin films

J. J. Mei, H. Chen, and W. Z. Shen^{a)}

Laboratory of Condensed Matter Spectroscopy and Opto-Electronic Physics, Department of Physics, Shanghai Jiao Tong University, 1954 Hua Shan Road, Shanghai 200030, People's Republic of China

H. F. W. Dekkers

Silicon Solar Cells Group, Microsystems, Components, and Packaging Division, IMEC vzw, Kapeldreef 75, B-3001 Leuven, Belgium

(Received 12 May 2006; accepted 17 July 2006; published online 13 October 2006)

We report on the optical properties and local bonding configurations of both as-deposited and postannealed hydrogenated amorphous silicon nitride ($a\text{-SiN}_x\text{:H}$) thin films grown on crystalline Si substrates with x approximately 1.2 ± 0.1 . Ultraviolet optical reflection and infrared (IR) absorption measurements were applied to characterize the films. A method simply based on optical reflection spectra is proposed for accurate determination of the optical band gap, band tail, wavelength-dependent refractive index and extinction coefficient, as well as the film thickness, suggesting that the Tauc-Lorentz [G. E. Jellison, Jr. and F. A. Modine, *Appl. Phys. Lett.* **69**, 371 (1996); **69**, 2137 (1996)] model with the inclusion of Urbach tail is the optimal one to describe the optical response of $a\text{-SiN}_x\text{:H}$ films. The yielded optical parameters can be related well to the film microstructure as revealed by the IR absorption analysis. These results have implications for future deposition controlling and device applications. © 2006 American Institute of Physics.

[DOI: [10.1063/1.2356915](https://doi.org/10.1063/1.2356915)]

I. INTRODUCTION

In recent years, hydrogenated amorphous silicon nitride ($a\text{-SiN}_x\text{:H}$) thin films are of great interest due to their potential applications in optoelectronic devices such as active component in thin film transistors,¹ gate dielectric in metal-insulator-semiconductor field effect transistors,² and antireflection coatings (ARCs) in solar cells.^{3,4} In commercial silicon solar cell production, 90% of all the ARCs are $a\text{-SiN}_x\text{:H}$ due to their beneficial passivation properties originating from hydrogen released from silicon nitride after thermal treatment.⁴ Silicon nitride films can be prepared by a number of methods including plasma enhanced chemical vapor deposition (PECVD), low pressure chemical vapor deposition (LPCVD), and sputtering. Regardless of deposition method, optical properties including optical band gap, Urbach tail, and wavelength-dependent optical constants (absorption coefficient and refractive index) of $a\text{-SiN}_x\text{:H}$ thin films are crucial for designs and applications of relevant optoelectronic devices. However, no method has been reported to obtain simultaneously all of these important optical parameters for $a\text{-SiN}_x\text{:H}$ films, although there are various optical studies based on optical transmission,^{5,6} spectroscopic ellipsometry,⁷ and photoluminescence⁸ measurements. In particular, extracting optical properties of $a\text{-SiN}_x\text{:H}$ films grown on absorbing substrates via optical reflection spectra in the ultraviolet (UV) spectral region has been scarcely reported. Furthermore, though several dielectric function

models (DFMs) such as the Adachi model,⁹ the Forouhi-Bloomer (FB) model,¹⁰ and the Tauc-Lorentz (TL) model^{11,12} have been employed for the extraction of the optical constants of semiconductors and dielectrics, many of these DFMs explicitly ignore the effect of the Urbach tail, which actually plays a role in the optoelectronic properties of $a\text{-SiN}_x\text{:H}$.⁸ Therefore, an appropriate choice of the DFMs is necessary for studying the optical properties of $a\text{-SiN}_x\text{:H}$.

Another source of information concerning the microstructure is the infrared (IR) absorption spectra. In particular, information on local atomic bonding configurations involving Si, N, and H atoms in $a\text{-SiN}_x\text{:H}$ films can be obtained. It is widely accepted that in plasma-deposited silicon nitride films, hydrogen originating from the precursor gases (SiH_4 and NH_3) during the deposition process may be bonded to nitrogen and silicon. The release of this bonded hydrogen involves lattice reaction and network rearrangement. However, although extensive research work has been reported in the literature about the bonding configurations^{13,14} and optical properties¹⁵ of $a\text{-SiN}_x\text{:H}$ films, little is known about the correlation between them. Therefore, it is useful to establish a relationship between the film microstructures of the $a\text{-SiN}_x\text{:H}$ and their macroscopic optical properties.

In this work, we propose a method for reliable determination of optical properties of $a\text{-SiN}_x\text{:H}$ in the UV region considering the Urbach tail by simply employing the optical reflection spectra. The yielded optical parameters can be related well to the local bonding configurations revealed by the IR absorption analyses, which helps to explore the microstructure of $a\text{-SiN}_x\text{:H}$ and will facilitate future deposition control.

^{a)}Author to whom correspondence should be addressed; electronic mail: wzshen@sjtu.edu.cn

TABLE I. Parameters of a -SiN_x:H films: the deposition temperature T_d , the NH₃/SiH₄ flux ratio, and the experimental film thickness d obtained by interferometry; the fitted thickness d_f , the demarcation energy between the Urbach tail transitions and the band-to-band transitions E_c , the band gap energy E_g , the Urbach Tail E_U , the amplitude A , the transition energy E_{0TL} , the broadening parameter C , and constant $\epsilon_{1\infty}$ in the TLU model; the Tauc gap E_{Tauc} deduced from the TLU absorption coefficient results; and the single oscillator energy E_0 and the dispersion energy E_d in the WD model.

Sample	T_d (°C)	NH ₃ /SiH ₄ (SCCM/SCCM)	d (nm)	d_f (nm)	E_c (eV)	Tauc-Lorentz model with Urbach tail							WD Model		
						E_g (eV)	E_U (meV)	A	E_{0TL} (eV)	C	$\epsilon_{1\infty}$	E_{Tauc}	E_0 (eV)	E_d (eV)	
As-deposited	Si300	300	1900/450	408	405	3.66	2.93	330	47.4	6.85	3.85	2.45	3.43	7.85	27.1
	Si400	400	1900/410	429	423	3.51	3.20	147	56.9	7.40	2.89	2.21	3.68	8.26	29.4
	Si500	500	1900/370	396	400	3.59	3.38	100	72.5	8.16	1.60	1.62	3.73	9.26	33.5
Annealed	Si300A	300	1900/450	418	420	3.52	2.99	249	53.5	7.87	2.89	1.69	3.48	8.25	26.4
	Si400A	400	1900/410	434	429	3.48	3.28	98	63.9	8.42	1.77	1.43	3.72	8.54	29.2
	Si500A	500	1900/370	406	425	3.66	3.51	71	73.3	9.09	0.41	1.13	3.77	9.46	33.1

II. EXPERIMENTAL DETAILS

Hydrogenated amorphous silicon nitride layers as typically used for ARCs of solar cells were deposited at different temperatures on ~ 0.5 mm thick p -type (10Ω cm) crystalline Si (c -Si) substrates of 10×10 mm² in size. A typical large throughput reactor was used with direct low frequency (440 kHz) plasma generation and relatively high deposition temperatures. The a -SiN_x:H alloys with film thickness of 380–420 nm were deposited at temperatures (T_d) of 300–500 °C and postannealed for 30 min at a moderate temperature of 690 °C. In order to keep the composition ratio N/Si in the film approximately equal to 1.2 ± 0.1 , the NH₃/SiH₄ flux ratio was slightly enhanced with the increase of T_d during the deposition process, thus the refractive index n at 632.8 nm remained close to 2.0, which is beneficial for relevant solar cell applications.⁴ The N/Si ratios were confirmed by x-ray photoelectron spectroscopy (XPS) made on a THETA 300 system and elastic recoil detection analysis (ERDA) measurement using a Walvis chamber at Debye Institute of Utrecht University. As we will discuss and demonstrate in Sec. IV, the effect of T_d plays a predominant role in determining the majority of optical and IR properties of the a -SiN_x:H investigated here, compared with that of NH₃/SiH₄ ratio adjustment, whereas the latter factor primarily induces the variations of N/Si ratio, N concentration, and N–H bond concentration (see Sec. IV B). The detailed deposition parameters are summarized in Table I. The UV optical reflection spectra were measured in the range of 2500–4000 Å using a Jobin Yvon 460 monochromator with a resolution of 2 Å. The IR absorption spectra were performed on a Nicolet Nexus 870 Fourier transform infrared spectrometer from 400 to 4000 cm⁻¹ with a resolution of 4 cm⁻¹. All the measurements were carried out at room temperature.

III. THEORETICAL METHOD

Optical constants (refractive index n and extinction coefficient k) of a material (either in bulk or thin film form) as a function of photon energy E (or wavelength λ) are important for both basic science and device applications. Optical properties of any medium can be described by the complex

index of refraction, $N = n - ik$, or the complex dielectric function, $\epsilon = \epsilon_1 - i\epsilon_2$. ϵ is related to N by $\epsilon = N^2$, so that $\epsilon_1 = n^2 - k^2$ and $\epsilon_2 = 2nk$. Optical characterization of materials supplies information about the optical constants, as well as optical band gap, band tail, band structure, optically active defects, etc. Thus, nondestructive measurements such as optical transmission and/or reflection, spectroscopic ellipsometry, and photoluminescence for determination of optical constants of each individual film in a multilayer structure can provide very valuable data. In general, optical reflection measurement is superior to optical transmission in the case of thick absorbing substrates. Since our a -SiN_x:H thin films of wide band gap (around 3–4 eV) were deposited on thick absorbing Si substrates, the optical reflectance spectra in the UV region are measured in order to investigate their optical band gap, band tail, wavelength-dependent refractive index and extinction coefficient, together with the film thickness.

Up to now, the extraction of the optical constants using the optical reflection spectra alone is usually very infrequent and complicated. The conventional envelope method based on the reflection extremes suggested by Minkov¹⁶ is only applicable to weakly absorbing thin films deposited on non-absorbent transparent substrates, whose refractive index is presumed to be a constant within the whole spectral range. The actual dispersion of the refractive index and absorption of the substrate adds difficulty and complexity to such kind of spectral analysis. In addition, this envelope method is an empirical one to determine the refractive index and extinction coefficient of the films without considering the Kramers-Kronig consistency. Therefore, the complex and diverse optical properties of materials investigated require more universal reflection equations and analysis methods.

Here, we adopt a general reflection equation which takes into account the wavelength-dependent refractive index and extinction coefficient of the substrate for an air/film/substrate/air configuration. Our method assumes that an optical reflection of an ideal parallel-sided thin film on a thick partly absorbing substrate is illuminated at nearly normal incidence with monochromatic radiation. The isotropic homogeneous film with average film thickness d_f is characterized by the complex refractive index $N_1 = n_1 - ik_1$ and the

substrate (with the thickness $\gg d_f$) by the complex refractive index $N_2 = n_2 - ik_2$. The total optical reflectance $R(\lambda)$ in this system is given by¹⁷

$$R(\lambda) = \frac{A + Bx + Cx^2}{D + Ex + Fx^2}, \quad (1)$$

where $x = \exp(-\alpha d_f)$ is the absorbance, $\alpha = (4\pi k_1)/\lambda$ is the absorption coefficient, $\phi = (4\pi n_1 d_f)/\lambda$,

$$\begin{aligned} A &= [(1 - n_1)^2 + k_1^2][(n_1 + n_2)^2 + (k_1 + k_2)^2], \\ B &= 2[A' \cos \phi + B' \sin \phi], \\ C &= [(1 + n_1)^2 + k_1^2][(n_1 - n_2)^2 + (k_1 - k_2)^2], \\ D &= [(1 + n_1)^2 + k_1^2][(n_1 + n_2)^2 + (k_1 + k_2)^2], \\ E &= 2[C' \cos \phi + D' \sin \phi], \\ F &= [(1 - n_1)^2 + k_1^2][(n_1 - n_2)^2 + (k_1 - k_2)^2], \\ A' &= (1 - n_1^2 - k_1^2)(n_1^2 - n_2^2 + k_1^2 - k_2^2) + 4k_1(n_1 k_2 - n_2 k_1), \\ B' &= 2(1 - n_1^2 - k_1^2)(n_1 k_2 - n_2 k_1) - 2k_1(n_1^2 - n_2^2 + k_1^2 - k_2^2), \\ C' &= (1 - n_1^2 - k_1^2)(n_1^2 - n_2^2 + k_1^2 - k_2^2) - 4k_1(n_1 k_2 - n_2 k_1), \\ D' &= 2(1 - n_1^2 - k_1^2)(n_1 k_2 - n_2 k_1) + 2k_1(n_1^2 - n_2^2 + k_1^2 - k_2^2). \end{aligned} \quad (2)$$

The simulation of the experimental reflection spectra using the above equations is based on the following steps:

- (i) Choose a DFM which describes $\varepsilon_1(\lambda)$ and $\varepsilon_2(\lambda)$ [or $n_1(\lambda)$ and $k_1(\lambda)$] of the film studied.
- (ii) Determine “best-fit” values of the fitting parameters including d_f and those involved in the DFM by minimizing the difference between the experimental (R_{exp}) and theoretical (R_{theo}) reflection spectra, i.e.,

$$\sum_i^{\text{all}} \{R_{\text{exp}}(\lambda_i) - R_{\text{theo}} \times [\lambda_i, n_1(\lambda_i), k_1(\lambda_i), d_f, n_2(\lambda_i), k_2(\lambda_i)]\}^2,$$

via the least-squares regression analysis. During the simulation, the $n_2(\lambda)$ and $k_2(\lambda)$ of the *c*-Si substrate in the UV region at room temperature are already taken from the standard database.

After the previous steps, the theoretical reflection spectra for all of our *a*-SiN_x:H thin films together with the fitted parameters can be obtained. The fitted curves using several DFMs are plotted in Fig. 1 for a typical *a*-SiN_x:H film and will be discussed below.

IV. RESULTS AND DISCUSSION

A. Optical reflection spectra

DFMs are preferred in the extraction of optical properties not only due to their Kramers-Kronig consistency, but also because of their convenient analytic representation of

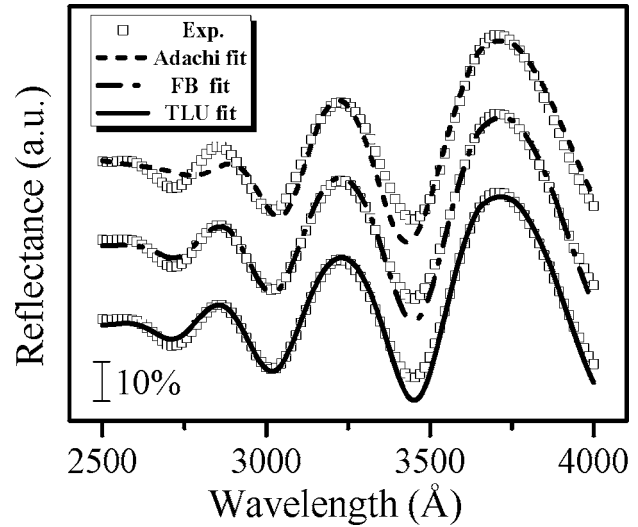


FIG. 1. The experimental (open scatters) and fitted optical reflectance spectra (dashed curve: yielded by the Adachi model; dash-dotted curve: yielded by the FB model; and solid curve: yielded by the TLU model) of as-deposited *a*-SiN_x:H sample Si300.

the semiconductor dielectric response. In contrast, empirical formulas for optical constants⁶ are discarded here, since they are not consistent with Kramers-Kronig relation. If the DFM cannot yield directly the values of optical band gap and Urbach tail, we can resort to the following so-called Tauc rule⁶ and exponential absorption equation⁸ for obtaining these two parameters:

$$\alpha(E) = \begin{cases} \frac{\alpha_0}{E}(E - E_{\text{Tauc}})^2, & E \geq E_{\text{Tauc}} \text{ (Tauc rule)} \\ \alpha_t \exp[(E - E_t)/E_U], & E < E_t \text{ (Urbach tail)}, \end{cases} \quad (3)$$

where E_{Tauc} is the optical band gap (Tauc gap), E_U is the Urbach tail, and α_0 , α_t , and E_t are constants.

We now take a typical sample Si300 as an example for comparison among several DFMs. As shown in Fig. 1, the fit by the Adachi model⁹ (dashed curve) is found not to agree with the experimental data (open scatters) very well in the whole spectral region, especially in the high energy region. Furthermore, the yielded E_U of 729 meV and d_f of 490 nm significantly deviate from the reliable values ($E_U \sim 300$ meV as indicated by other methods^{18,19} and $d = 408$ nm obtained by interferometry for sample Si300). We also take the FB model¹⁰ into account. The agreement between FB model simulation (dash-dotted curve) and experimental spectrum seems to be achieved over the entire range of photon energy. Nevertheless, the yielded $k(E)$ is usually unreasonable below the band gap and hence it is difficult to derive a reliable band tail, as implied by its extinction coefficient equation. In 1996, Jellison and Modine summarized the limitations of the FB model and proposed a Tauc-Lorentz (TL) model.^{11,12} However, this TL model is commonly applicable in the interband region and does not consider the absorption caused by the Urbach tail. In fact, the Urbach tail in hydrogenated amorphous silicon nitride can be up to more than 300 meV and its effect cannot be disregarded. There-

fore, we choose the TL model with inclusion of the exponential Urbach tail and the assumption of continuous first derivative of dielectric function²⁰ (denoted as the “TLU model” hereinafter) to describe more accurately the optical properties of $a\text{-SiN}_x\text{:H}$ layer. The TLU model is an improved version of the original TL model. The fit given by the TLU model (solid curve) not only reproduces well the experimental data, but also yields reasonable band tail (330 meV), band gap ($E_{\text{Tauc}}=3.427$ eV), film thickness (405 nm), as well as the optical constants for Si300. The same goes to other $a\text{-SiN}_x\text{:H}$ samples investigated in this work. As a result, we think that the TLU model is the optimum one for the extraction of optical properties in $a\text{-SiN}_x\text{:H}$.

In the TLU model, the imaginary part of the complex dielectric function is defined by

$$\varepsilon_2(E) = \begin{cases} \frac{1}{E} \frac{AE_{0\text{TL}}C(E-E_g)}{(E^2-E_{0\text{TL}}^2)^2+C^2E^2}, & E \geq E_c \\ \frac{A_U}{E} \exp\left(-\frac{E}{E_U}\right), & 0 < E < E_c, \end{cases} \quad (4)$$

where the first term (photon energy $E \geq E_c$) is identical to the Tauc-Lorentz function and the second term ($0 < E < E_c$) represents the exponential Urbach tail.²⁰ E_c , E_g , A , $E_{0\text{TL}}$, and C denote the demarcation energy between the Urbach tail transitions and the band-to-band transitions, the band gap energy, the amplitude, the transition energy, and the broadening parameter, respectively. A_U and E_U are chosen with respect to boundary continuity of the optical function including the first derivative. This leads to the relations

$$E_U = (E_c - E_g) \left[2 - 2E_c(E_c - E_g) \frac{C^2 + 2(E_c^2 - E_{0\text{TL}}^2)}{C^2E_c^2 + (E_c^2 - E_{0\text{TL}}^2)^2} \right]^{-1}, \quad (5)$$

$$A_U = \exp\left(-\frac{E_c}{E_U}\right) \frac{AE_{0\text{TL}}C(E_c - E_g)}{(E_c^2 - E_{0\text{TL}}^2)^2 + C^2E_c^2}. \quad (6)$$

The real part $\varepsilon_1(E)$ is determined by the Kramers-Kronig transformation as a closed form given in Ref. 20. The total seven fitting parameters are E_c , E_g , A , $E_{0\text{TL}}$, C , $\varepsilon_{1\infty}$ [appearing in the expression of $\varepsilon_1(E)$], and the film thickness d_f .

Figure 2 shows the experimental (open scatters) and fitted (solid curves) reflection spectra for all of our $a\text{-SiN}_x\text{:H}$ samples using the Tauc-Lorentz-Urbach (TLU) model. The relevant absorption coefficient α and refractive index n are shown in Fig. 3. The fitted variables of TLU model, the Urbach tail E_U , and the yielded Tauc gap E_{Tauc} by fitting $\alpha(E)$ to Eq. (3) are listed in Table I. It is obvious that the fitted film thickness d_f is very close to the experimental value, which partially validates our method. On the other hand, the E_{Tauc} values are closely comparable to those of $a\text{-SiN}_x\text{:H}$ with x of ~ 1.2 reported in Ref. 18, further supporting the use of the TLU model.

Then, we begin to analyze the fitted results. In the as-deposited $a\text{-SiN}_x\text{:H}$ films, the band gap parameter E_g is smaller than E_{Tauc} by Tauc extrapolation, due to the empirical nature of the TL model.²¹ Both E_{Tauc} and E_g increase with increasing T_d , while the band tail E_U shows an opposite

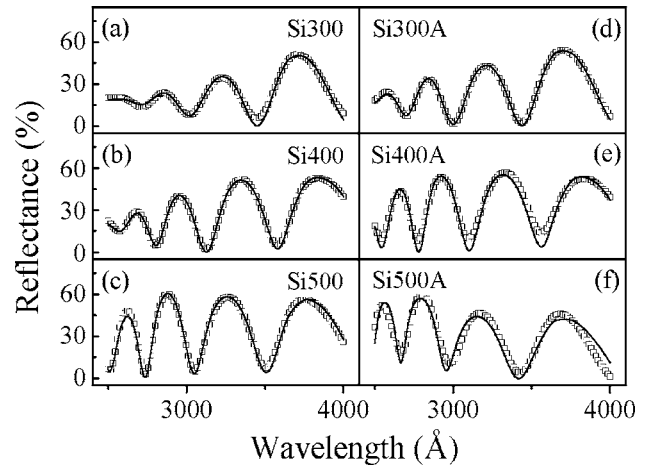


FIG. 2. Experimental optical reflectance spectra (open scatters) of all the as-deposited and annealed $a\text{-SiN}_x\text{:H}$ samples, together with theoretical fits (solid curves) by the TLU model.

trend. Meanwhile, the light absorption effect becomes weaker at higher T_d in the UV region due to the variation of E_{Tauc} with T_d [see Fig. 3(a)]. This phenomenon is coincident with the E_U and C (a broadening parameter related to disorder) behaviors and suggests that the film is more ordered at the higher T_d . In contrast, the refractive indices n at given wavelengths are found to increase with increasing T_d . As shown typically in Fig. 3(c), the refractive indices n at 632.8 nm extrapolated from the fitted parameters are 2.054, 2.074, and 2.113 for samples Si300, Si400, and Si500, respectively. The annealed samples Si300A, Si400A, and Si500A experience similar changes of the aforementioned optical properties versus T_d . Notice that the increase of

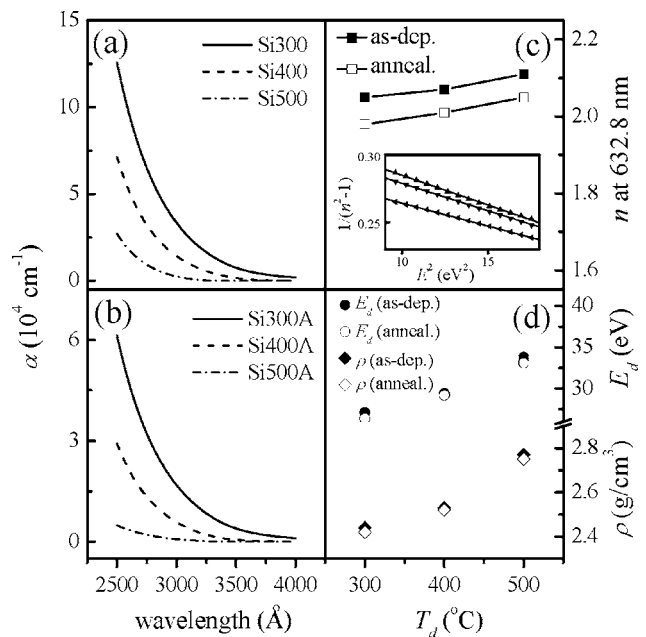


FIG. 3. Wavelength-dependent absorption coefficient α for the (a) as-deposited and (b) annealed $a\text{-SiN}_x\text{:H}$ films, respectively. (c) Refractive indices n of $a\text{-SiN}_x\text{:H}$ films at 632.8 nm as functions of T_d . Plots of factor $(n^2-1)^{-1}$ vs E^2 for the subgap n of samples Si300 (\blacktriangle), Si400 (\blacktriangledown), and Si500 (\blacktriangleleft) together with the linear fits (solid lines) are typically shown in the inset of (c). (d) The dependence of E_d and ρ on T_d .

NH_3/SiH_4 ratio generally enhances E_U (Ref. 18) and reduces n ,¹⁴ which is opposite to our observations. This reflects that T_d is a dominant factor in determining these optical parameters.

Next, we turn to discuss the annealing effect. Compared with the as-deposited samples, the annealed ones exhibit larger band gaps (E_g and E_{Tauc}), smaller band tail E_U , and smaller C , which indicates that annealing induces more order within $a\text{-SiN}_x\text{:H}$. Also, the refractive index and the absorption coefficient simultaneously decrease after annealing as displayed in Figs. 3(b) and 3(c), respectively. About 50% of absorption reduction is observed while the refractive index decreases slightly after annealing. The fitted film thickness becomes slightly thicker after annealing and may lead to the decrease of the film density, primarily due to the thermal expansion effect. Similar expansion phenomenon of film thickness has also been observed in Ref. 19 for the film with N/Si ratio x of 1.43.

Finally, of particular interest is that the subgap (mainly below E_{Tauc} or E_g , sometimes below $E_{0\text{TL}}$) refractive-index behavior (magnitude and dispersion) deduced from the TLU fitting parameters for all of the $a\text{-SiN}_x\text{:H}$ samples, whether annealed or not, are found to obey remarkably the one-oscillator Wemple-DiDomenico (WD) model²² of the form

$$n^2(E) - 1 = E_0 E_d / (E_0^2 - E^2), \quad (7)$$

with E_0 the single oscillator energy and E_d the dispersion energy, as illustrated by the inset of Fig. 3(c). The relevant results of E_0 and E_d are listed in Table I. E_0 , which is comparable to the transition energy $E_{0\text{TL}}$, is typically near the main peak of the imaginary part of dielectric function ϵ_2 . It reflects the energy difference between the ‘‘centers of gravity’’ of the valence and conduction bands, indicative of an average gap of the material. This average gap gives quantitative information on the ‘‘overall’’ band structure, differing from the conventional optical gap such as Tauc gaps which probes optical properties near the fundamental band gap of the material.²¹ Parameter E_d , which is a measure of the strength of interband optical transitions and nearly independent of E_0 , mainly reveals information about mass density and coordination number. Therefore, these two WD parameters help us to gain insights into the material microstructure. Both E_0 and $E_{0\text{TL}}$ exhibit nearly the same trend with the variation of T_d . Besides, annealing results in the increase of average band gap in $a\text{-SiN}_x\text{:H}$. The E_d will be further related to mass density ρ calculated from the IR absorption results (see Sec. IV B) as shown in Fig. 3(d) and will be discussed in Sec. IV C.

B. IR absorption spectra

Figure 4(a) shows the infrared absorption spectrum in the range from 400 to 4000 cm^{-1} for the film layer of sample Si300, where the substrate absorption contribution has been subtracted through dividing the sample transmission spectrum by that of a bare $c\text{-Si}$ substrate. Notice that interference effects in the films have already been removed from the spectra via a base line correction process. The absorption bands have been assigned as follows: N–H (stretching) mode

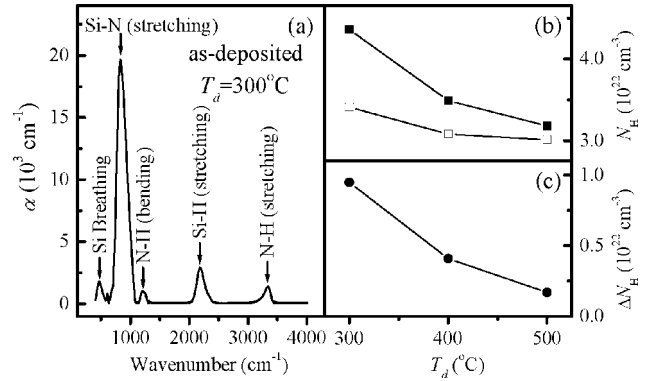


FIG. 4. (a) IR absorption spectrum of the film layer for the as-grown $a\text{-SiN}_x\text{:H}$ prepared at $T_d=300$ °C. (b) The bonded hydrogen concentration N_H before (solid squares) and after (open squares) annealing, and (c) the amount of evolved hydrogen ΔN_H upon annealing (solid circles) vs T_d .

near 3330 cm^{-1} , Si–H (stretching) mode near 2190 cm^{-1} , N–H (bending) mode near 1200 cm^{-1} , Si–N (stretching) mode near 850 cm^{-1} , Si–H (bending) mode near 610 cm^{-1} , and Si breathing mode near 480 cm^{-1} .

The concentrations of Si–N, Si–H, and N–H bonds in these alloys can be obtained from the normalized infrared absorption bands by

$$N_{X-Y} = K_{X-Y} \int_{400}^{4000} \alpha(\nu) d\nu, \quad (8)$$

where N_{X-Y} is the concentration of X – Y bond and K_{X-Y} is their infrared absorption cross section calibration factor. Values of $K_{\text{Si-H}}=5.9 \times 10^{16} \text{ cm}^{-1}$ and $K_{\text{N-H}}=8.2 \times 10^{16} \text{ cm}^{-1}$ have been taken from the results of Lanford and Rand²³ using $K=1/(2.303\sigma)$ with σ the absorption cross section.²⁴ Considering the N/Si ratios to be approximately 1.2 in our $a\text{-SiN}_x\text{:H}$ samples as revealed by XPS and ERDA measurements, the value of $K_{\text{Si-N}} \approx 2.2 \times 10^{16} \text{ cm}^{-1}$ is used according to Ref. 14. Then, the atom concentrations N_{Si} , N_{N} , N_{H} , and mass density ρ can be calculated from the following expressions derived by Yin and Smith²⁴ assuming the absence of N–N and H–H bonds in the films:

$$\begin{aligned} N_{\text{Si}} &= [N_{\text{Si-N}} + N_{\text{Si-H}}]/4 + N_{\text{Si-Si}}/2, \\ N_{\text{N}} &= [N_{\text{Si-N}} + N_{\text{N-H}}]/3, \\ N_{\text{H}} &= N_{\text{Si-H}} + N_{\text{N-H}}, \\ \rho &= m_{\text{Si}}N_{\text{Si}} + m_{\text{N}}N_{\text{N}} + m_{\text{H}}N_{\text{H}}, \end{aligned} \quad (9)$$

where the m_i are atomic masses. The relevant results of both the as-deposited and annealed samples are summarized in Table II. It is clear from Table II that the $N_{\text{Si-N}}$, $N_{\text{N-H}}$, and ρ increase, while $N_{\text{Si-H}}$ decreases with the increasing T_d . In contrast to those of Refs. 25 and 26 the variations of $N_{\text{N-H}}$ and N/Si ratio are mainly ascribed to the intentional adjustment of NH_3/SiH_4 ratio at different T_d during the deposition process. Figures 4(b) and 4(c) show the bonded hydrogen concentration N_H and related change ΔN_H upon annealing versus T_d , respectively, which clearly indicate that both N_H and ΔN_H decrease significantly with increasing T_d . Since the

TABLE II. Bond and atom concentrations, and mass density ρ for a -SiN_x:H films obtained from IR absorption spectra.

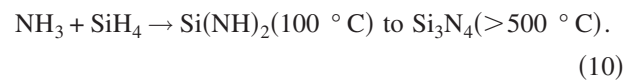
Samples	$N_{\text{Si-N}}^a$ (10^{22} cm^{-3})	$N_{\text{Si-H}}^a$ (10^{22} cm^{-3})	$N_{\text{N-H}}^a$ (10^{22} cm^{-3})	N_{Si} (10^{22} cm^{-3})	N_{N} (10^{22} cm^{-3})	N_{H} (10^{22} cm^{-3})	N/Si	H/Si	ρ (g/cm ³)
Si300	9.10	2.63	1.53	3.21	3.74	4.36	1.16	1.35	2.44
Si400	9.75	1.70	1.60	3.29	4.04	3.49	1.23	1.06	2.53
Si500	11.02	1.05	1.94	3.54	4.62	3.18	1.30	0.90	2.77
Si300A	10.03	2.71	0.47	3.29	3.63	3.41	1.10	1.04	2.42
Si400A	10.27	2.04	0.82	3.36	3.90	3.08	1.16	0.91	2.52
Si500A	11.38	1.20	1.61	3.53	4.57	3.01	1.29	0.85	2.75

^aBond concentrations of Si–N (stretching) mode near 850 cm⁻¹, Si–H (stretching) mode near 2190 cm⁻¹, and N–H (stretching) mode near 3330 cm⁻¹.

increase of NH₃/SiH₄ ratio will lead to the enhancement of N_{H} ,²⁴ the observations illustrated by Fig. 4 reveal that the reduction of N_{H} and ΔN_{H} are mainly due to the increase of T_d .

In order to ascertain the structural changes induced by deposition temperature, the local bonding configurations of the as-grown films with different T_d are further investigated. Figures 5(a)–5(c) show the overall Si–N stretching absorbance of as-deposited alloys, which have been deconvoluted into three Gaussian bands centered at about 820, 900, and 1015 cm⁻¹. These three bands are assigned to symmetric stretching mode of N₂–Si–H₂ group, Si–N asymmetric stretching mode, and symmetric stretching mode of N₃–Si–H group, respectively.²⁷ The fitted peaks of each Si–N absorption band are 804, 894, and 996 cm⁻¹ for Si300; 810, 900, and 999 cm⁻¹ for Si400; and 822, 921, and 1014 cm⁻¹ for Si500. It should be noted that the Si–N fre-

quencies increase monotonically with T_d , which can be elucidated by the following chemical reactions²⁸ for NH₃ and SiH₄ at different deposition temperatures:



According to this reaction, there are two different local bonding configurations of Si(NH)₂ and Si₃N₄ at the nitrogen atom sites incorporated into the films at the intermediate deposition temperatures (300–500 °C). The infrared studies also show that there is a continuous and smooth transition between the silicon diimide [Si(NH)₂] structure and the silicon nitride (Si₃N₄) structure, which is accompanied by a loss of hydrogen and more incorporation of nitrogen. The difference in the Si–N stretching mode frequencies in Si(NH)₂ and Si₃N₄ has two possible origins: (1) change in the bond angle at the nitrogen atom site from approximately 128° in the Si(NH)₂ to 120° in Si₃N₄, and (2) an increase of the Si–N force constant from diimide to the nitride, which shortens the Si–N bond lengths. This increase of force constant is anticipated from the differences in the Si–N bond lengths between trisilylamine (1.738 Å) and silazane (1.725 Å).²⁸ Consequently, the smaller the bond angle and the shorter the Si–N bond length, the higher the wave number of the Si–N absorption peak. The variations of the bond angle and length can be interpreted to originate from the process of the bond interchange reaction and the nitrogen atom electronic orbital hybridization. In Si(NH)₂, N is bonded to two silicon atoms and one hydrogen atom, and the most stable configuration is the sp^3 tetrahedral hybridization. In Si₃N₄, the nitrogen will be bonded to three silicon atoms, and the interaction between the doubly occupied p_z nonbonding orbital perpendicular to the bond plane and the internal type d orbital of the three silicon atoms now make the sp^2 planar hybridization of the nitrogen atom highly stable.²⁹ Hence, the blueshift of as-grown Si–N absorption band indicates the above structural rearrangement induced by deposition temperature, and shows that it is physically more stable for alloys deposited at higher temperature.

However, though these parameters of annealed films have the same trends as the as-grown ones depending on T_d , the $N_{\text{Si-H}}$ and $N_{\text{Si-N}}$ are enhanced while the $N_{\text{N-H}}$ becomes smaller after the annealing process. We interpret these variations as evidences for the following well-known chemical ordering reaction:³⁰

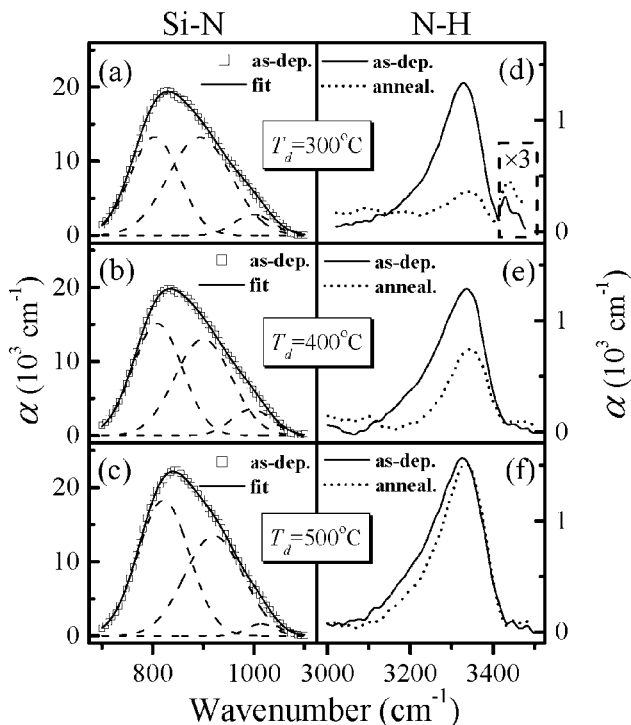
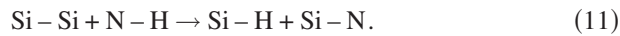
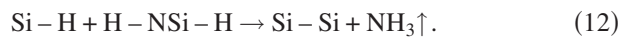


FIG. 5. (a)–(c) Experimental (open scatters) and fitted (solid curves) absorption spectra of the Si–N stretching mode for the three as-deposited a -SiN_x:H films. (d)–(f) The observed absorption spectra of N–H stretching mode for the a -SiN_x:H films before (solid curves) and after annealing (dotted curves).



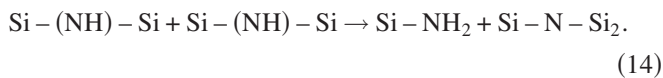
In addition, the loss of both hydrogen and nitrogen atomic concentrations in the annealing process can also be proposed as:¹⁹



Another reaction³¹ may also be responsible for the hydrogen release:



Figures 5(d)–5(f) illustrate the N–H absorption bands of the as-grown and annealed films. Deeper inspection of the N–H stretching mode around 3350 cm⁻¹ reveals two asymmetrical features aside from the main N–H peak: a tail on the low wave number side and a shoulder on the high wave number side. The former one may be attributed partly to the intermolecular hydrogen bonding formed by the N–H groups, indicative of incomplete nitridation of the *a*-SiN_{*x*}:H thin film during deposition. The latter one is due to the stretching modes of N–H₂ unit between 3400 and 3500 cm⁻¹. It is obvious that the N–H absorptions are reduced and the corresponding peaks blueshift after annealing, which implies the change of local bonding configurations from NH to NH₂ mode. This can be explained by the reaction



The distinct enhancement of NH₂ absorption near 3450 cm⁻¹ for sample Si300A [Fig. 5(d)] further substantiates the above arguments and reaction (14). This conversion is apparently one of the steps leading to the formation and subsequent evolution of NH₃ molecules from the annealed film.²⁴ However, since the NH₂ participates in reaction (12) to create NH₃, the increase of NH₂ absorption in the other two annealed films are not as prominent as in Si300A. In other words, the lower the deposition temperature, the larger the reduction and blueshift of the N–H absorption bands in the annealed samples compared to those of as-deposited ones.

It is worthwhile to mention that the H release process is reduced at higher *T_d* films. Both the bonded hydrogen concentration *N_H* and the amount of evolved *N_H* (i.e., Δ*N_H*) induced by annealing decrease significantly with increasing *T_d*, as shown in Figs. 4(b) and 4(c), respectively. The behavior of Δ*N_H* is related to the microstructure and stability of films, i.e., the higher the *T_d*, the stabler the film and the less the H dissociation after annealing in *a*-SiN_{*x*}:H. However, previous work³² has pointed out that the reduction of Δ*N_H* is not directly related to the observed bulk and surface passivations of multicrystalline solar cells. Instead, it suggests that the degree of passivation improves when *a*-SiN_{*x*}:H films are denser and thermally stabler. Dekkers *et al.*³³ have also observed similar phenomenon and achieved a conclusion that for *a*-SiN_{*x*}:H layers with higher density more hydrogen is directly available for passivation. This implies higher *T_d* is beneficial for fabrication of device-quality *a*-SiN_{*x*}:H.

C. Further discussion

Now we relate optical results deduced from the optical reflection spectra with the IR absorption data.

It has been proposed¹⁴ that the refractive index of *a*-SiN_{*x*}:H alloys can be represented as the bond-density-weighted linear combination of reference refractive indices taken at *x*=0 and at *x*=4/3. Therefore, the N/Si ratio can be evaluated by the refractive index of the silicon nitride films by using

$$x = \frac{\text{N}}{\text{Si}} = \frac{4}{3} \frac{n_{a\text{-Si:H}} - n}{n + n_{a\text{-Si:H}} - 2n_{a\text{-Si}_3\text{N}_4}} = \frac{4 \cdot 3.3 - n}{3n - 0.5}, \quad (15)$$

with refractive indices at 632.8 nm *n_{a-Si:H}*=3.3 for *a*-Si:H and *n_{a-Si₃N₄}*=1.9 for nearly stoichiometric *a*-Si₃N₄, where hydrogen bonding has been neglected. Alternatively, it can be determined by using the equation

$$x = \frac{\text{N}}{\text{Si}} = \frac{0.70}{n - 1.39}, \quad (16)$$

as suggested in Ref. 34. Both methods are in fairly good agreement with each other after using the derived refractive indices from optical reflection spectra for our *a*-SiN_{*x*}:H films; the yielded ratio is near 1.1, which is very close to IR calculation and accurate ERDA or XPS measurements.

However, the calculated N/Si ratio using Eqs. (15) and (16) decreases with increasing *n*, which is opposite to the IR results in our samples. This contradiction may be attributed to the exclusion of *T_d* effect in Eqs. (15) and (16). It has already been pointed out in Ref. 34 that the refractive index changes from 1.9 to 2.0 with increasing *T_d* even at the same N/Si ratio. So it is significant for refractive index related equations to consider the effect of *T_d* on the density of the films. In terms of Lorentz-Lorenz effective medium theory,³⁵ we obtain

$$n^2 = 3f \left(1 - \frac{4\pi A_v}{3 \varepsilon_0} \alpha_e \frac{\rho}{M} \right) - 2, \quad (17)$$

where *n*, *M*, *ρ*, *A_v*, *ε₀*, and *α_e* are refractive index, molecular weight, density, Avogadro's number, dielectric constant of free space, and average electronic polarizability, respectively. Sinha and Lugujo³⁵ reported that the (α_e)_{Si} was a function of the N/Si ratio, i.e., 10²⁴(α_e)_{Si}=1.67+1.39/*x* cm⁻³ for the films with 0.62<*x*<1.33, whereas (α_e)_N is assumed to remain constant at 0.35×10⁻²⁴ cm⁻³ for all films. Therefore, the N/Si ratio (mainly related to NH₃/SiH₄ ratio) should be taken into account, which influences the molecular weight and average electronic polarizability in Eq. (17). Since 1/*M* and *α_e* roughly decrease with increasing *x*, the enhancement of refractive index at higher *T_d* reflects dominantly the increase of density, which is again confirmed by relevant results calculated from the IR data. Increasing deposition temperature is known to densify the film and thus increase *n*,²⁵ while raising NH₃/SiH₄ ratio has an opposite effect on *n*.¹⁴ Therefore, the experimental observation of the enhancement of *n* at higher *T_d* indicates that the deposition temperature is a relatively more important parameter than NH₃/SiH₄ ratio in determining *n* in our *a*-SiN_{*x*}:H samples, analogous to the case of achieving low surface recombination velocity.³⁶

Deeper insight into the film microstructure is provided by the WD parameter E_d obtained from the refractive index dispersion, which follows a simple empirical relationship $E_d = \beta N_c Z_a N_e$ in a variety of crystalline covalent and ionic solids and liquids, with β , Z_a , and N_e constants depending on the material, and N_c the coordination number of the cation nearest neighbor to the anion. The WD model was extended to amorphous semiconductor and dielectrics by proposing a relation $E_d^a/E_d^b = (\rho^a/\rho^b)(N_c^a/N_c^b)$, where a and b refer to amorphous and crystalline forms, respectively. Therefore, E_d mainly reveals information about density and coordination number. Note that the N atom has a chemical preference to be bonded to three Si atoms^{37,38} and the *ab initio* calculation reveals that the average number of nearest neighbor Si around N atom is approximately 3.0 for all the range of x .³⁹ Thus the E_d reflects primarily the behavior of the density ρ . Figure 3(d) shows the comparison between E_d (Table I) and ρ obtained from IR data (Table II), which directly confirms the consistency between the reflection and IR results.

The E_U behavior mainly reflects the degree of disorder in the network of a -SiN_{*x*}:H, which is known to be affected by both NH₃/SiH₄ ratio^{8,18} and T_d . The higher the N content or the lower the T_d , the larger the E_U . In spite of the increased N/Si ratio in these films, the Urbach tail does not increase appreciably but decreases with increasing T_d . This suggests that the deposition temperature is a more important factor during film growth. Besides, the full width at half maximum (FWHM) of Si–N stretching band obtained from the IR spectra of the films is indicative of the disorder in the network.¹⁹ The FWHM parameters are 204.7, 201.1, and 197.4 cm⁻¹ for samples Si300, Si400, and Si500, respectively, while 191.7, 188.7, and 186.4 cm⁻¹ for the corresponding annealed ones. The reduction of E_U upon annealing reveals that the a -SiN_{*x*}:H films become more ordered, consistent with the above FWHM results.

The calculated Tauc gap E_{Tauc} is in connection with the H diffusion a -SiN_{*x*}:H according to Ref. 18, where it has been proposed that the H diffusion activation energy E_a for diffusion increases in direct proportion to E_{Tauc} . Higher E_a at higher T_d hinders H diffusion, which helps to explain why the bonded H loss is less at higher T_d as shown in Fig. 4(c) and discussed in Sec. IV B. Nevertheless, more work is still needed to clarify the mechanism of H diffusion and related passivation of Si surface and bulk defects.

V. CONCLUSIONS

We have systematically investigated the optical properties and local bonding configurations of both as-deposited and postannealed a -SiN_{*x*}:H alloys ($x \sim 1.2 \pm 0.1$) grown on c -Si substrates by PECVD, using the UV optical reflection and the IR absorption spectra. A theoretical method is proposed for an air/film/substrate/air configuration to determine the wavelength-dependent refractive index n and extinction coefficient k , optical band gap, Urbach tail, and the film thickness, simply using the experimental reflection spectra. Several DFMs are inspected and compared, among which the TLU model is chosen for the optimal extraction of those important optical parameters. The E_{Tauc} , E_g , and n are found

to increase with increasing deposition temperature T_d , while the E_U and α behave contrarily. The annealing further enhances E_{Tauc} and E_g , and reduces E_U and α . The TLU-yielded subgap refractive indices are related well to the WD model whether annealed or not, which provides insights into the specific microstructure of the films through parameter E_0 and E_d .

The IR absorption results reveal the concentrations of Si–N, Si–H, and N–H bonds and of Si, N, and H atoms in the a -SiN_{*x*}:H, as well as the local bonding evolution upon annealing. The Si–N (stretching) and N–H (stretching) bond changes of different a -SiN_{*x*}:H films are ascribed to the local bonding transitions and network relaxations. The transition from Si(NH)₂ structure to Si₃N₄ structure within a -SiN_{*x*}:H lowers bond angle and shortens Si–N bond length, and thus blueshifts the Si–N stretching absorption peak. In the annealing process, the change of local bonding configurations from NH to NH₂ mode causes the reduction of N–H absorption and the blueshift of corresponding peak. The bonded H content is reduced and H release upon annealing becomes less easy but more effective in passivation at higher T_d , implying that higher deposition temperature is more beneficial to both Si surface and bulk passivation.

Finally, the connection between the optical reflection and IR results is established, which not only confirms the consistency and reliability of the optical reflection and IR analyses, but also provides a basis for future deposition controlling and device applications of a -SiN_{*x*}:H.

ACKNOWLEDGMENTS

This work was supported by the Natural Science Foundation of China under Contract Nos. 60576067 and 10674094, the National Minister of Education Program for Changjiang Scholars and Innovative Research Team in University (PCSIRT), and Shanghai Municipal Commission of Science and Technology Project Nos. 05QMH1411 and 06JC14039.

- ¹S. S. He, M. J. Williams, D. J. Stephens, and G. Lucovsky, *J. Non-Cryst. Solids* **164–166**, 731 (1993).
- ²D.-G. Park, Z. Chen, A. E. Botchkarev, S. N. Mohammad, and H. Morkoç, *Philos. Mag. B* **74**, 219 (1996).
- ³R. Hezel and R. Schörner, *J. Appl. Phys.* **52**, 3076 (1981).
- ⁴F. Duerinckx and J. Szlufcik, *Sol. Energy Mater. Sol. Cells* **72**, 231 (2002).
- ⁵M. Molinari, H. Rinnert, and M. Vergnat, *Appl. Phys. Lett.* **77**, 3499 (2000).
- ⁶H. Chen, M. H. Gullanar, and W. Z. Shen, *J. Cryst. Growth* **260**, 91 (2004).
- ⁷S. Zollner and E. Apen, *AIP Conf. Proc.* **550**, 532 (2001).
- ⁸H. Kato, N. Kashio, Y. Ohki, K. S. Seol, and T. Noma, *J. Appl. Phys.* **93**, 239 (2003).
- ⁹S. Adachi, *Phys. Rev. B* **43**, 12316 (1991).
- ¹⁰A. R. Forouhi and I. Bloomer, *Phys. Rev. B* **34**, 7018 (1986).
- ¹¹G. E. Jellison, Jr. and F. A. Modine, *Appl. Phys. Lett.* **69**, 371 (1996).
- ¹²G. E. Jellison, Jr. and F. A. Modine, *Appl. Phys. Lett.* **69**, 2137 (1996).
- ¹³S. Hasegawa, M. Matsuda, and Y. Kurata, *Appl. Phys. Lett.* **58**, 741 (1990).
- ¹⁴E. Bustarret, M. Bensouda, M. C. Habrard, J. C. Bruyère, S. Poulin, and S. C. Gujrathi, *Phys. Rev. B* **38**, 8171 (1988).
- ¹⁵E. A. Davis, N. Piggins, and S. C. Bayliss, *J. Phys. C* **20**, 4415 (1987).
- ¹⁶D. A. Minkov, *J. Phys. D* **22**, 1157 (1989).
- ¹⁷J. Müllerová and J. Mudroň, *Acta Phys. Slov.* **50**, 477 (2000).

- ¹⁸J. Robertson, *Philos. Mag. B* **69**, 307 (1994).
- ¹⁹F. L. Martínez, A. del Prado, I. Mártel, G. González-Díaz, B. Selle, and I. Sieber, *J. Appl. Phys.* **86**, 2055 (1999).
- ²⁰M. Foldyna, K. Postava, J. Bouchala, J. Pištora, and T. Yamaguchi, *Proc. SPIE* **5445**, 301 (2004).
- ²¹H. Chen and W. Z. Shen, *Eur. Phys. J. B* **43**, 503 (2005).
- ²²S. H. Wemple and M. DiDomenico, Jr., *Phys. Rev. B* **3**, 1338 (1971).
- ²³W. A. Lanford and M. J. Rand, *J. Appl. Phys.* **49**, 2473 (1978).
- ²⁴Z. Yin and F. W. Smith, *Phys. Rev. B* **42**, 3666 (1990).
- ²⁵M. T. K. Soh, N. Savvides, C. A. Musca, M. P. Martyniuk, and L. Faraone, *J. Appl. Phys.* **97**, 093714 (2005).
- ²⁶M. Maeda and Y. Arita, *J. Appl. Phys.* **53**, 6852 (1982).
- ²⁷J. Bandet, B. Despax, and M. Caumont, *J. Appl. Phys.* **85**, 7899 (1999).
- ²⁸D. V. Tsu, G. Lucovsky, and M. J. Mantini, *Phys. Rev. B* **33**, 7069 (1986).
- ²⁹F. L. Martínez *et al.*, *Thin Solid Films* **459**, 203 (2004).
- ³⁰Z. Yin and F. W. Smith, *Phys. Rev. B* **43**, 4507 (1991).
- ³¹K. C. Lin and S. C. Lee, *J. Appl. Phys.* **72**, 5474 (1992).
- ³²J. Hong, W. M. M. Kessels, W. J. Soppe, A. W. Weeber, W. M. Arnoldbik, and M. C. M. van de Sanden, *J. Vac. Sci. Technol. B* **21**, 2123 (2003).
- ³³H. F. W. Dekkers, L. Cernel, and G. Beaucarne, *Appl. Phys. Lett.* **89**, 013508 (2006).
- ³⁴W. A. P. Claassen, W. G. J. N. Valkenburg, F. H. P. M. Habraken, and Y. Tamminga, *J. Electrochem. Soc.* **130**, 2419 (1983).
- ³⁵A. K. Sinha and E. Lugujo, *Appl. Phys. Lett.* **32**, 245 (1978).
- ³⁶L. Cai, A. Rohatgi, S. Han, G. May, and M. Zou, *J. Appl. Phys.* **83**, 5885 (1998).
- ³⁷C. Cunha, S. Canuto, and A. Fazzio, *Phys. Rev. B* **48**, 17806 (1993).
- ³⁸P. P. M. Venezuela and A. Fazzio, *Phys. Rev. Lett.* **77**, 546 (1996).
- ³⁹F. de Brito Mota, J. F. Justo, and A. Fazzio, *J. Appl. Phys.* **86**, 1843 (1999).